https://doi.org/10.5194/egusphere-2022-1004
Preprint. Discussion started: 6 October 2022

New ring shear deformation apparatus for three-dimensional multiphase experiments: First results

Shae McLafferty[1], Haley Bix[1], Kyle Bogatz[1], Jacqueline E. Reber[1]

[1]Department of Geological and Atmospheric Sciences, Iowa State University, Ames, Iowa, 50011, USA

Correspondence to: Jacqueline Reber (jreber@iastate.edu)

Key words: Ring shear apparatus, HydroOrbs, Hydrogel spheres, Semi-brittle experiments, granular experiments

Abstract

Multiphase deformation, where a solid and fluid phase deform simultaneously, play a crucial role in a variety of geological hazards, such as landslides, glacial slip, and the transition from earthquakes to slow slip. In all these examples a continuous, viscous or fluid-like phase is mixed with a granular or brittle phase where both phases deform simultaneously when stressed. Understanding the interaction between the phases and how they will impact deformation dynamics is essential to improve hazard assessments for a wide variety of geo-hazards. Here, we present the design and first experimental results from a ring shear deformation apparatus capable of deforming multiple phases simultaneously. The experimental design allows for three dimensional observations during deformation in addition to unlimited shear strain, controllable normal force, and a variety of boundary conditions. To impose shear deformation, either the experimental chamber or lid rotate around its central axis while the other remains stationary. Normal and pulling force data are collected with force gauges located on the lid of the apparatus and between the pulling motor and the experimental chamber. Experimental materials are chosen to match the light refraction index of the experimental chamber, such that 3D observations can be made throughout the experiment with the help of a laser light sheet. We present experimental results where we deform hydropolymer orbs and cubes (brittle phase) and Carbopol® hydropolymer gel (fluid phase). Preliminary results show variability in force measurements and deformation styles between solid and fluid end member experiments. The ratio of solids to fluids and their relative competencies in multiphase experiments control deformation dynamics, which range from stick-slip to creep. The presented experimental strategy has the potential to shed light on multi-phase processes associated with multiple geo-hazards.

Plane language abstract (500 characters incl. space)

Multiple geologic hazards, such as landslides and earthquakes, arise when solids and fluids coexist and deform together. We designed an experimental apparatus that allows to observe such deformation in 3D. The first results show how fluids and solids deform and break at the same time allowing us to study the impact of both materials on deformation distribution and speed. Making these processes visible has the potential to improve risk assessments associated with geological hazards.

https://doi.org/10.5194/egusphere-2022-1004
Preprint. Discussion started: 6 October 2022

1 Introduction

Multiple geo-hazards result from three key ingredients: A solid phase that can fracture unstably, a fluid phase that influences the state of stress and can have a viscosity spanning many orders of magnitude, and a driving force such as gravity or tectonics. For example, on hillslopes, incipient shear of sediments creates volume change, which in turn causes the pore-water flow and the associated stress changes that govern the stability of landslides (e. g., Iverson et al., 2000). At crustal scales, the proportions of solid to fluid phases and their interactions can modulate deformation dynamics and lead to a spectrum of behaviour from earthquakes to slow slip events (e. g., Fagereng and Sibson, 2010; Behr and Bürgmann, 2021; Kirkpatrick et al., 2021). In addition, syn-deformation solid-fluid interactions control slip rates at the beds of ice sheets (e. g., Iverson et al., 1995; Zoet and Iverson, 2020) — the single most significant uncertainty in predicting dynamic contributions of ice sheets to sea-level rise over the next century as the climate warms (Stocker and Others, 2013; Rignot et al., 2019). In all these examples a continuous, viscous or fluid-like phase is mixed with a granular or brittle phase where both phases deform simultaneously when stressed. Understanding the interaction between the phases and how they will impact deformation dynamics is crucial to improve the hazard assessments for a wide variety of geo-hazards.

While there are many experimental (Ladd and Reber, 2020; Reber et al., 2014; Higashi and Sumita, 2009) and numerical studies (Ioannidi et al., 2022; Jammes et al., 2015; Ioannidi et al., 2021; Behr et al., 2021) that investigate different aspects of two-phase or brittle-viscous interactions, they face multiple challenges and limitations. To resolve the complex interaction of the brittle and viscous phase, high resolution experiments or simulations are necessary. In addition, the materials need to be able to deform in different manners independently of each other. This means that the brittle material loses cohesion when failure occurs while the viscous material flows under stress. Furthermore, the impact of simultaneous two-phase deformation is inherently a three-dimensional problem. Numerical experiments are suitable to evaluate two-phase systems in 3D where it is possible to make continuous observations. In addition, systematic parameter studies are feasible. However, the resolution of numerical models, especially in 3D is strongly dependent on available computational resources. But perhaps the greatest drawback of numerical models is the difficulty of having two phases where one is continuous and the other is able to break and therefore becoming discontinuous. The simultaneous deformation of two fundamentally different phases is trivial in physical experiments, as is the resolution issue. While the scaling of experiments using analogue materials remains a challenge, a further hurdle is the observation in 3D. It is difficult to make observations in 3D without the need to destroy the experiment by slicing it open and therefore limiting the deformation progression.

Here, we present the design of a new ring shear deformation apparatus that allows deformation of multiphase experiments to be monitored in 3D. Besides the apparatus design, data acquisition process, and 3D visualization of experiments, we present the first data gathered with the device to demonstrate its versatility and potential applications.

https://doi.org/10.5194/egusphere-2022-1004
Preprint. Discussion started: 6 October 2022

2 Shear apparatus

2.1 Apparatus design

The apparatus has no theoretical limits on applied strain, it has controllable normal force (confining pressure), and is combined with an optical setup to make observations of internal deformation while the experiment is in progress. The apparatus consists of an experimental chamber, a hydraulically controlled lid that exerts a normal force, and a motor that initiates shear by rotating the experimental chamber (Table 1). The material chamber is built with two concentric transparent cylinders to form a ring-shaped gap (an annulus in a two-dimensional plan view). The radii of the cylinders are 19 cm and 11 cm for the outer and inner cylinders, respectively, resulting in an 8 cm wide annulus. Both cylinders have a height of 16 cm, of which approximately 14 cm can be filled with the experimental materials. The cylinders are sealed to a baseplate at the bottom thus both the cylinders and baseplate move as a unit during deformation. The apparatus is designed so that the experimental chamber can be turned while the lid remains stationary, leading to a Eulerian observational system in which the observation window is stationary while the experimental material passes through it. This allows for the observation of spatial variability. However, the apparatus can be configured in such a way that the experimental chamber is stationary and the lid turns. This allows for Lagrangian observations in which the evolution of one parcel of the material can be observed during increasing shear deformation.

A hydraulically controlled lid can be lowered between the walls of the experimental chamber and onto the experimental materials to exert a normal force (Figure 1). The hydraulic system controls the lid to either exert a constant pressure or hold the lid at a constant position. The gaps between experimental chamber and the lid are sealed with o-rings that are lubricated with grease to reduce friction between the chamber walls and the lid. Normal force is recorded with a force gauge connected to the top of the lid.

An electromagnetic rotary motor encompasses the baseplate of the experimental chamber (grey circle in Figure 1) and rotates at a steady angular velocity. The motor is connected to the experimental chamber (Figure 1) to transfer motion. The difference in motion between the lid and the material chamber results in shear of the experimental materials. Eight teeth, 1 cm high and wide, transverse both the lid and baseplate and help to transfer motion onto the experimental material. The most relevant specification and sources of third-party components used to build this machine are listed in Table 1.

https://doi.org/10.5194/egusphere-2022-1004
Preprint. Discussion started: 6 October 2022

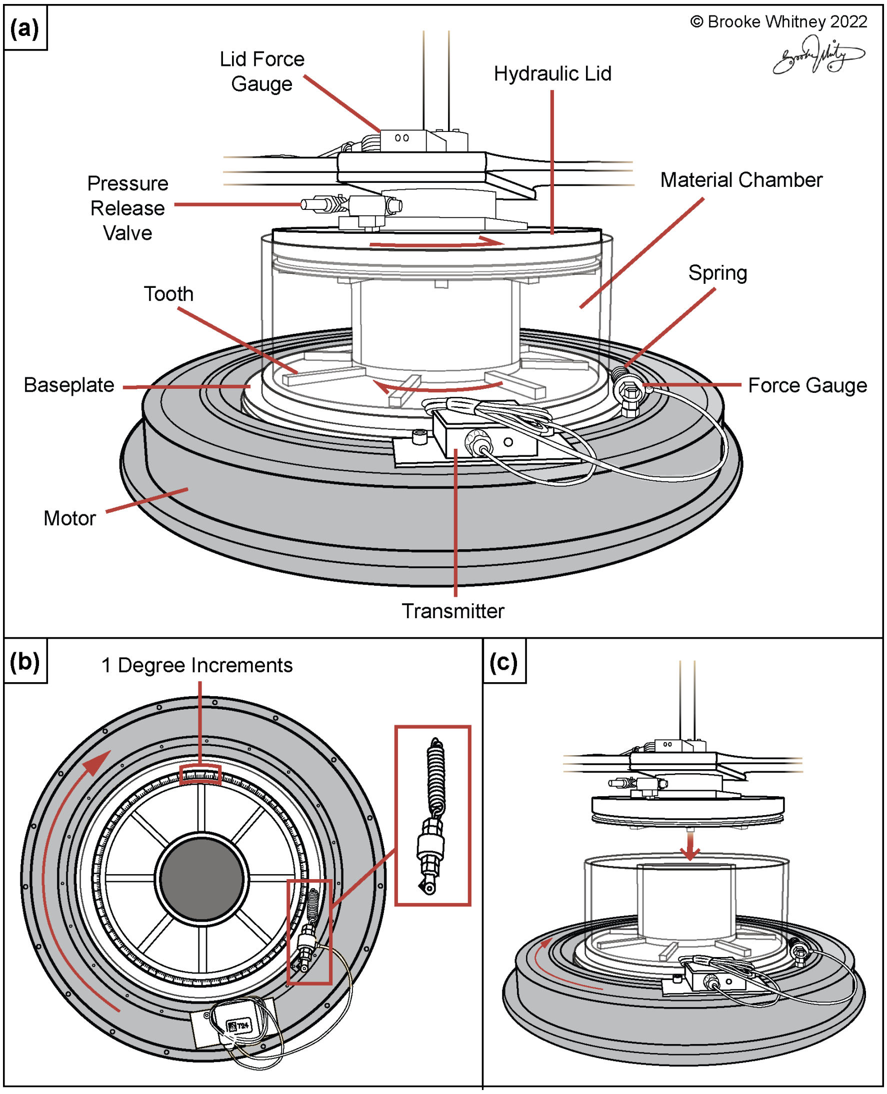

Figure 1: Illustration of the ring shear apparatus named *Shearknado*. a) Labelled side view of the apparatus with the lid lowered into the experimental chamber. b) Plan view of the experimental chamber and surrounding motor with a close-up of spring and force gauge configuration. c) Side view of the apparatus. Illustration credit to ©Brooke Whitney 2022.

https://doi.org/10.5194/egusphere-2022-1004
Preprint. Discussion started: 6 October 2022

Table 1: Source and most relevant specifications of parts provided by third party sellers for the shear apparatus.

	Source:	Specifications:
Direct drive rotary servo table	Intelidrives	max. velocity: 108 rpm
Air-powered high-cycle, high-flow hydraulic system	Milwaukee Cylinder	Pressure: 11000-16000 kPa
Amplified load cell (normal force)	Interface	Sensor capacity: 69000 kPa
Miniature in-line load cell (pulling force)	Applied measurements	max. load: 100 N
Diode pumped green laser	CrystaLaser	Wavelength: 532 nm
		Output power: 100 mW

2.2 Boundary condition

The ring shear apparatus allows for either a constant strain rate or an energy conserving boundary condition. For the constant strain rate boundary condition, the experimental chamber is connected directly to the motor with a force gauge in between. The force gauge records the bulk force required to rotate the material chamber, and the strain rate is set by the rotation velocity of the motor. Conversely, the energy conserving boundary condition neither prescribes the strain rate nor the stress (Birren and Reber, 2019; Daniels and Hayman, 2009; Reber et al., 2014). In this case, the experimental chamber is connected to the force gauge and the motor via a spring (Figure 1b). Adding the spring creates a boundary condition that allows for strain rate and force to vary as the spring extends or contracts in response to material deformation (Figure 2 a). Continuous deformation, or creep, in the material chamber results in a relatively smooth force signal. The spring first elastically loads, increasing the pulling force until the spring is fully loaded, followed by minimal oscillation of the spring. Conversely, frictional deformation or stick-slip in the material chamber results in noticeable spring oscillation after initial loading. Shear within the experimental chamber only occurs once the frictional resistance of the apparatus and the experimental material strength are overcome. This leads to repeated increases of force followed by decreases resulting in stick-slip like motion (Figure 2 a).

Force gauge measurements are taken at a frequency of 10 Hz. The recorded force signal is dependent on the stiffness of the spring (Figure 2 b and c) and has to be chosen according to the weight of the experimental material. At a minimum, the spring needs to be strong enough to be able to pull the loaded experimental chamber. A large spring constant will lead to smaller and sharper peaks in the force curve where, in an extreme case, a constant strain rate boundary condition is approached. A small spring constant leads to a noisier signal. For the experiments presented here, we chose a spring with a constant of 9712 N/m. This spring constant and force measurement frequency combination ensures we can fully capture any force signal resulting from material deformation from creep to stick-slip, including transient deformation.

https://doi.org/10.5194/egusphere-2022-1004
Preprint. Discussion started: 6 October 2022

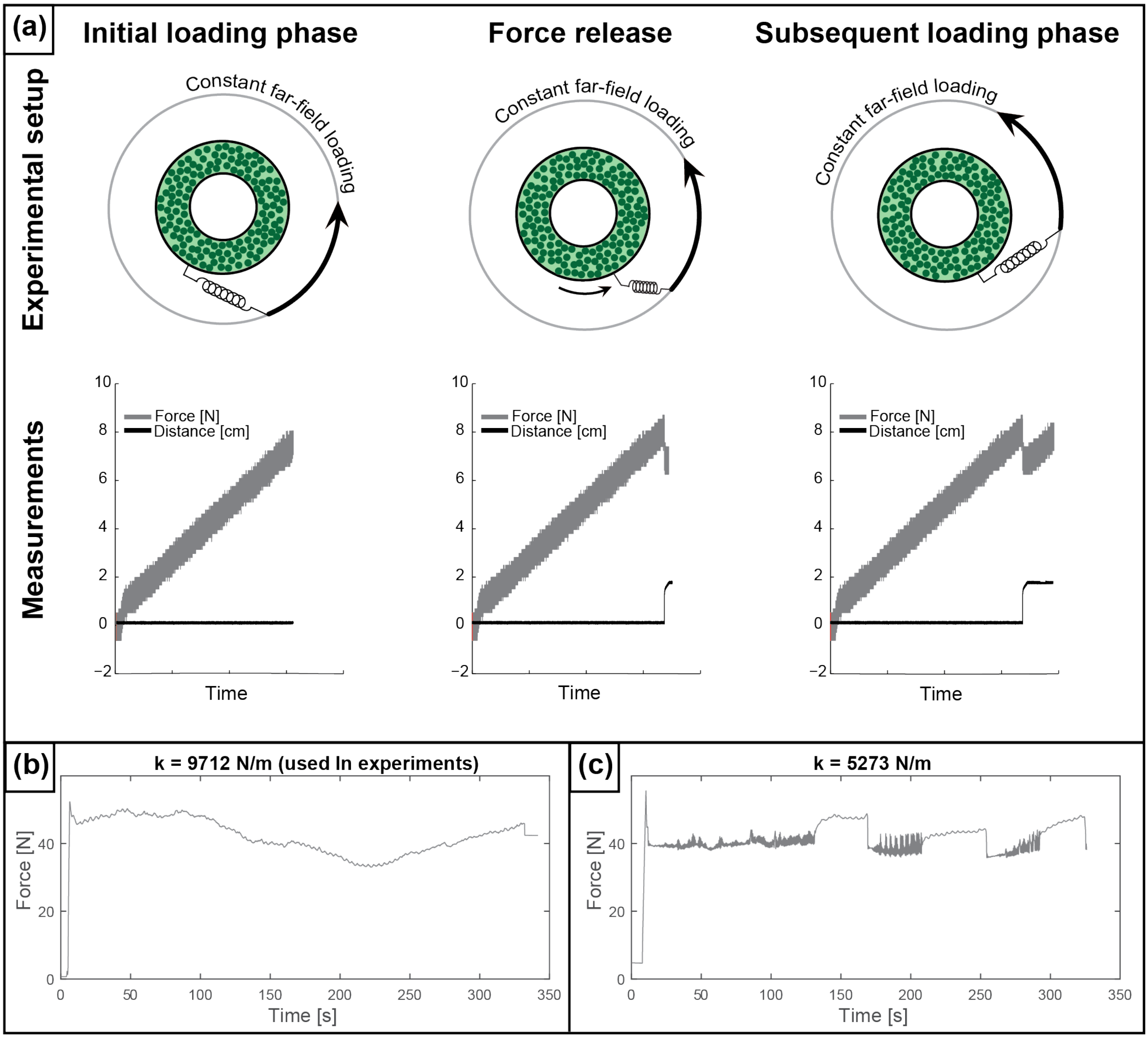

Figure 2: a) Schematic illustration of the energy conserving boundary condition. (Left) Initial loading accumulates force until slip occurs. (Middle) Slip-event results in force drop and sharp increase in displacement. (Right) Subsequent loading accompanied by an increase in force and no motion. b) Force measurement from semi-brittle experiment using a spring with spring constant k = 9712 N/m. c) Force measurement from same experiment with spring constant k = 5273 N/m.

2.3 Observation of internal deformation

The experimental chamber walls are made of transparent acrylic plastic allowing for 360-degree observation of the experiment (Figure 3). To document the deformation within the chamber we take advantage of the almost identical light refraction indices of the experimental materials and the experimental chamber (Budwig, 1994; Byron and Variano, 2013; Klein et al., 2013;

https://doi.org/10.5194/egusphere-2022-1004
Preprint. Discussion started: 6 October 2022

Dijksman et al., 2017). Material mixtures with identical or very similar light refraction indices allow light to travel through the entire experimental chamber. If the refraction indices of the individual phases are different, one phase will cast a shadow and/or scatter the light and obscure the other phase. Glass, transparent acrylic plastic, Carbopol, and HydroOrbs (for detailed material properties see section 3) have light refraction indices close to 1.3 (Auernhammer et al., 2020; Parker and Merati, 1996). This makes any mixture of these materials indistinguishable in natural light. Illumination with a laser light sheet, however, makes the different phases visible due to small differences in the light refraction indices (Figure 4). While the difference in light refraction indices between materials is large enough to make the different phases visible in laser light, it is small enough to not cast any shadows, resulting in the illumination of an entire slice through the experimental chamber (Mukhopadhyay and Peixinho, 2011).

The laser sheet originates from a 100 mW class 3B, 532 nm laser located 1 m from the experimental chamber (Figure 3 a). These specifications allow for the beam to illuminate an entire cross section of the experiment without excessive heating. To create the laser sheet, a series of optical lenses and mirrors are used to manipulate the beam (Figure 3 c and d). Alignment of the beam is controlled by using two 20 mm round silver mirrors placed at 45-degree angles from the beam path. Two spherical lenses with focal lengths of 50 mm and 200 mm are placed 150 mm apart within the final beam trajectory to magnify (4x) and collimate the beam. A -25 mm focal length convex cylindrical lens then expands the beam, forming a vertical sheet. A 1000 mm focal length spherical lens is the final optic placed in the beam path, 1m away from the experimental chamber, to create a narrow beam at the point of penetration into the experiment chamber. During experimentation, a camera is placed perpendicular to the laser sheet and captures cross sectional photos as the chamber rotates.

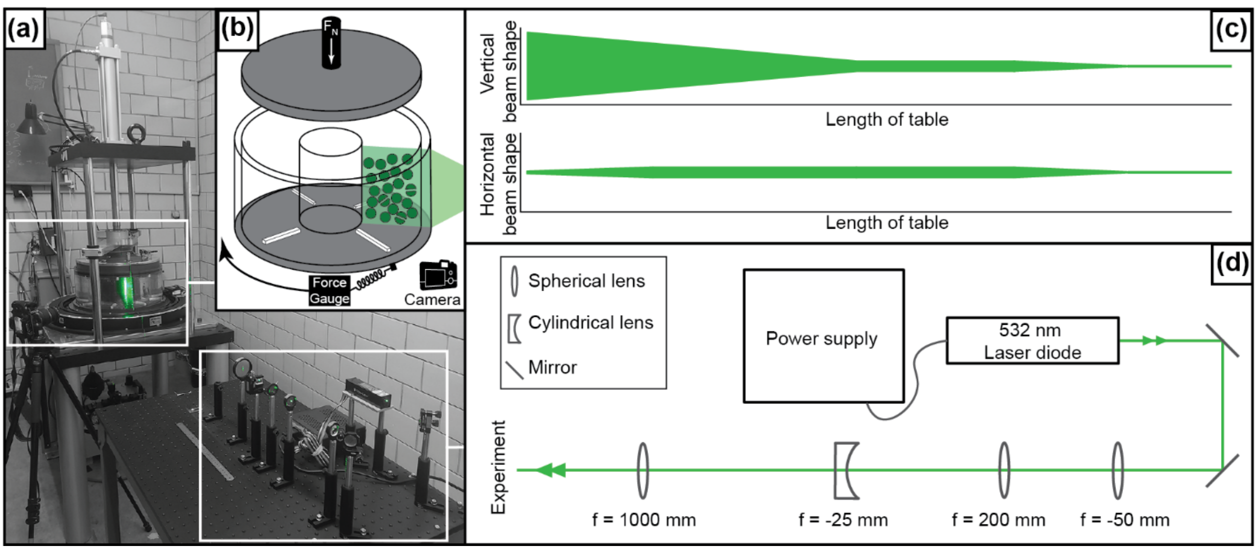

Figure 3: a) Photograph of experimental setup, b) closeup sketch of the experimental chamber with the laser sheet and camera position. c) Vertical and horizontal beam shape. d) Plan view showing the optical layout used to create the laser sheet. Over the length of the table, the first two lenses magnify and collimate the beam in both the vertical and horizontal planes. In the vertical direction, the third lense stretches the beam to create a laser sheet. The fourth lens thins the laser sheet in the horizontal plane.

https://doi.org/10.5194/egusphere-2022-1004
Preprint. Discussion started: 6 October 2022

3 Experimental materials

The experimental materials presented here are not an exhaustive list of all potential materials but a selection we have chosen to use. With experimental chamber walls made of transparent acrylic plastic all experimental materials must have similar optical properties to be visible within the experiment. So far, we have conducted experiments using Carbopol, HydroOrbs, and HydroCubes. While water has also a comparable light refraction index, we did not conduct experiments using water as its very low viscosity makes it difficult to avoid leakage.

3.1 Brittle phase (HydroOrbs and HydroCubes)

HydroOrbs, also known as polymer hydrogel spheres (e. g., James et al., 2020), and HydroCubes are elasto-plastic solids that deform elastically. Once a yield stress is reached they break (Figure 4). HydroOrbs, which are spherical in shape, and HydroCubes, which are cuboidal, begin as dehydrated plastic beads/cubes. Dehydrated HydroCubes are produced in large sheets, which can then be cut prior to hydration into desired size, shape, and aspect ratio. By this premise, HydroCubes need not be cubes, but rather may be of any desired shape. They are limited only by the volume of the original HydroCube sheet. When the orbs or cubes are placed in water, they incorporate H_2O into their structure and swell to about ten times their initial size. They reach their maximum volume after 1-4 days submerged in water. Once the orbs and cubes are fully hydrated, they are transparent. The volume of hydrated HydroOrbs is limited by the initial volume of the dehydrated plastic pellets, which come in small and large sizes. The final size of the orbs and cubes can be manipulated to some degree via the water salinity, where lower salinity leads to larger shapes (Table 2). We conduct experiments on both orbs and cubes that are soaked in either di-ionized water or tap water. The salinity of the water also has an impact on the yield stress of the orbs and cubes. In addition, the yield stress of the orbs and cubes can be lowered by cutting with a scalpel or puncturing with a needle. The puncture introduces a line of weakness by penetrating a rind of denser material in the outermost 1-2 mm of the orb (Chang et al., 2018). HydroCubes generally have a lower yield stress relative to the HydroOrbs, and, as a result, should not be hydrated with DI water as they often fracture during the hydration process.

3.2 Viscous phase (Carbopol)

We use a visco-elasto-plastic hydropolymer gel, Carbopol® as the viscous phase in the experiments. Carbopol is a transparent, non-linear yield stress fluid with a power law viscosity that can be approximated the Herschel-Bulkley model in equation 1 (Herschel and Bulkley, 1926; Di Giuseppe et al., 2015),

$$\sigma = \sigma_y + K_v \dot{\varepsilon}^n \tag{1}$$

where the stress, σ, is dependent on the yield stress, σ_y, the consistency index, K_v, the strain rate, $\dot{\varepsilon}$, and the flow index, n. The consistency index is a constant of proportionality between shear stress and strain rate where a higher consistency is a result of

https://doi.org/10.5194/egusphere-2022-1004
Preprint. Discussion started: 6 October 2022

a greater change in shear stress from a change in strain rate (Reber et al., 2020). Both the yield stress and viscosity of the Carbopol can be adjusted by changing the polymer concentration and pH of the Carbopol gel mixture, respectively. However, the properties of the Carbopol are held constant in the experiments presented here, with an average yield stress, σ_y, of 28.21 Pa and average viscosity of ~240 Pa.s. The flow index, n, is calculated from the slope of the linear relationship between the logarithm of strain rate and the logarithm of shear stress and is found to be 0.37.

Table 2: Experimental material properties.

Material Property	Small HydroOrb		Large HydroOrb	HydroCube	Carbopol®
Water	DI	Tap	Tap	Tap	DI
Volume (cm^3)	2.48 ± 0.45	1.54 ± 0.24	31.76 ± 8.27	-	-
Mass (g)	2.82 ± 0.43	1.73 ± 0.17	38.12 ± 11.27	-	-
Density (g/cm^3)	1.07 ± 0.05	1.08 ± 0.07	1.04 ± 0.06	1.05 ± 0.10	1018.00 ± 9.90
Viscosity (PaS)	-	-	-	-	101.76 - 448.91
Poisson's Ratio	0.39 ± 0.07	0.27 ± 0.08	0.37 ± 0.07	0.36 ± 0.10	-
Young's Modulus (kPa)	121.93 ± 57.59	143.72 ± 89.79	43.68 ± 23.16	19.72 ± 15.07	-
Shear Modulus (kPa)	42.98 ± 20.98	57.85 ± 38.36	16.78 ± 8.55	7.16 ± 5.58	-
Yield Stress (kPa)					
Non-punctured	72.27 ± 18.86	78.55 ± 21.93	15.01 ± 14.37	5.92 ± 2.43	0.01 - 0.05
Punctured	25.62 ± 16.25	21.97 ± 15.70	7.07 ± 12.79	-	-

https://doi.org/10.5194/egusphere-2022-1004
Preprint. Discussion started: 6 October 2022

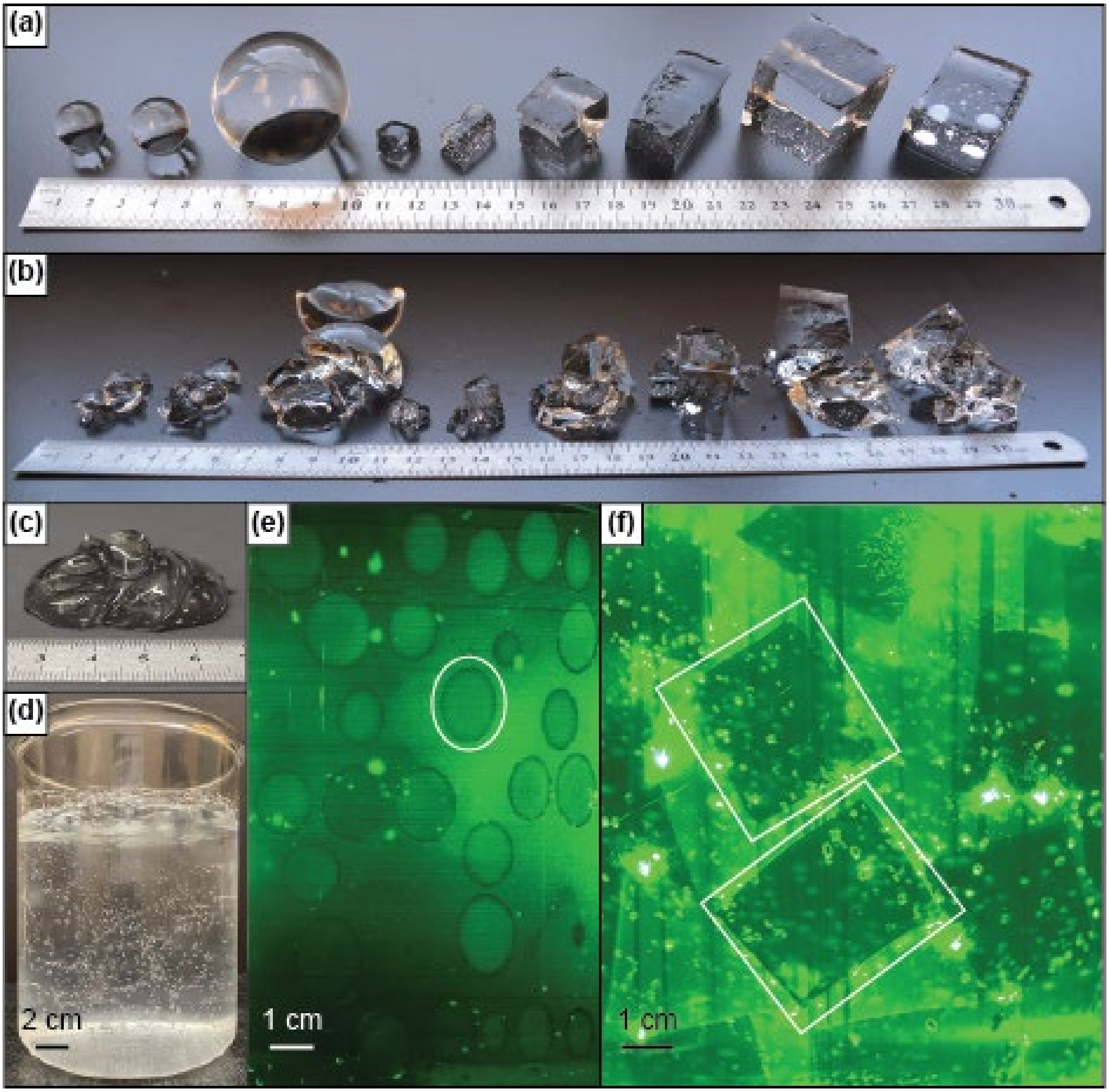

Figure 4: a) Fully hydrated HydroOrbs and HydroCubes. b) Fragmented HydroOrbs and HydroCubes after the yield stress is reached. c) Carbopol, d) Mixture of Hydrocubes and Carbopol in natural light, e) HyrdoOrb and Carbopol mixture illuminated by the laser sheet. f) HydroCube and Carbopol mixture illuminated by the laser sheet. Note bright small spots are due to the light reflection on trapped air bubbles.

https://doi.org/10.5194/egusphere-2022-1004
Preprint. Discussion started: 6 October 2022

4 Data acquisition

4.1 Visual documentation

Internal deformation in semi-brittle experiments, where both phases are present in the experimental chamber, is recorded throughout the experiment with photos of the illuminated cross section. 360 photos are taken every one degree around the material chamber (Figure 1) before the experiment, after every rotation for the first 10 rotations, and then after rotations 15 and 20. The 1-degree interval is small enough that every HydroOrb or HydroCube is captured in multiple photos and ensures fragments of the broken orbs or cubes are also captured. After each experiment, broken orbs or cubes are counted and their location within the illuminated cross section is recorded.

Cross-sectional photos only work for experiments where the entire experimental chamber is filled with material of similar light refraction indices. For all other experiments (brittle and viscous experiments), pictures are taken perpendicular to the experimental chamber wall.

4.2 Force measurements

Normal force measurements are recorded with the force gauge located on the hydraulically driven lid at a frequency of 100 Hz. To measure the pulling force, a force gauge is mounted in series with a spring between the experimental chamber and the rotating motor. The force gauge is connected to a wireless transmitter allowing for data collection over many rotations. The recorded pulling force is a bulk measurement consisting of the force required to deform the experimental material plus the frictional resistance of the experimental apparatus.

A background experiment is used to identify and separate the noise originating from machine friction from the signal of the deforming experimental material. The background experiment is performed by loading the experimental chamber with weights comparable to the weight of the experimental materials intended to deform during an experiment. The lid is lowered into the experimental chamber without touching the weights. This allows us to record the force needed to move the machine without deforming any experimental material. The raw force data from the background experiment is shown in Figure 5.

Multiple noise signatures are identified in the raw force data from the background experiment. Low-frequency oscillations in the raw data (Figure 5) are due to imperfect contact between the lid and the outer cylinder of the material chamber caused by a minuscule eccentricity of the cast acrylic cylinders (Bogatz, 2021). This results in orientations of the rotating cylinder where there is more friction between the lid and the outer cylinder resulting in a larger force required to rotate the experimental chamber. This imperfection leads to approximately one low-frequency wavelength per rotation. Another effect of non-constant friction between the lid and material chamber are very high frequency force oscillations lasting seconds to minutes (Figure 5). The high frequency jumps are caused by the spring oscillating in response to increased friction between the lid and the outer cylinder. In this case, an increase in friction causes a sticking event resulting in loading of the spring until slip occurs, reoccurring at a high frequency. Further, increased friction also manifests as irregular and sharp jumps in force surrounded by a relatively smooth force signal (Figure 5). Friction between the lid and the outer cylinder increases through time and therefore

https://doi.org/10.5194/egusphere-2022-1004
Preprint. Discussion started: 6 October 2022

causes more stick-slip motion and irregular force jumps with increased strain in the experiments. This limits the number of rotations in an experiment to approximately 20.

Other noise associated with normal machine operation includes abrupt decreases in the pulling force due to repositioning of the hydraulic lid. The position of the hydraulic lid is set at the beginning of the experiment. During the experiments, the lid sinks under its own weight and corrects its position approximately every 80 seconds (Bogatz, 2021). While the lid motion is only a fraction of a millimetre, it leaves a signature in the force data. Other abrupt decreases in force take place due to slipping between the lid and the outer cylinder. These decreases are generally greater than 5 N and often occur before the irregular jumps in force and smooth force signal outlined above. In addition to sharp jumps in force, elastic loading of the spring is included in the force signal every time the motor is stopped and starts to move again. The loading is shown as a drastic increase in force magnitude at the onset of the data collection (Figure 5). Lastly, we observe a low amplitude, high-frequency force oscillations that occur throughout the experiment. The amplitude of these oscillations is less than 0.5 N in the background experiment (Bogatz, 2021). These oscillations are extremely regular, repeat throughout the experiment, and are originating from the stepper motor.

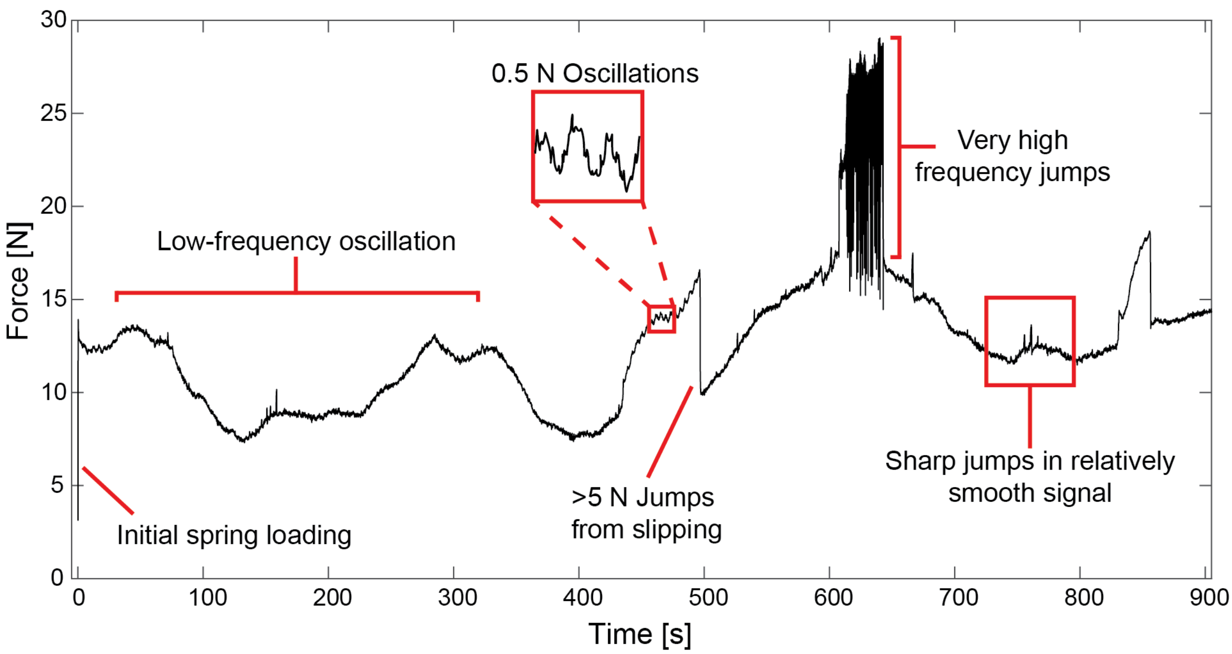

Figure 5: Raw force data from the Background experiment showing representative noise signals.

https://doi.org/10.5194/egusphere-2022-1004
Preprint. Discussion started: 6 October 2022

4.3 Data processing

Identifying the different styles of machine noise above allows us to remove them from the bulk force recorded during an experiment. To process the pulling force data from an experiment, the raw force data is first separated into individual rotations (Figure 6 a). We then cut out large and recognizable noise events such as the noise associated with friction between the lid and the outer cylinder, as well as the abrupt decreases in pulling force described above and initial elastic loading of the spring. We are left with samples of the force data that only have the low-frequency oscillation and the regular low-amplitude, high-frequency oscillations, in addition to the force signal from the deforming materials (Figure 6 b). In a next step, we use a Lowess filter in Matlab to remove the regular low-amplitude, high-frequency oscillations as well as the force signal associated with material deformation from the sample (Figure 6 b). The Lowess filter is a non-parametric fitting tool that creates a linear regression for the data points contained within a specified window size (Bogatz, 2021). Using a window size of 100 to filter the data ensures only the low frequency wavelengths associated with the imperfect contact between the lid and the outer cylinder is preserved. We then take the difference between the filtered and the raw data of the samples to obtain the force signal from the deforming materials (Figure 6 c).

At this point, the variance of the difference values can be calculated, illustrating the average spread of the data. Higher variance values are equivalent to larger differences between the total force measurement and the machine noise filter. The difference also includes the regular low-amplitude, high-frequency oscillations from the motor. However, this motor noise is present in all experiments and is subtracted from the experiment variance values by using the variance of the background experiment. Variance values from samples in one rotation are averaged and each average is plotted to determine the change in variance through time. A linear regression is fit though the points. In the background force experiment, the variance values decrease slightly through time (Figure 6 d). The variance values for each rotation in the background experiment are used to normalize results from experiments where we deform experimental materials.

To calculate the average pulling force magnitude for each machine rotation we take the average of the data points in each rotation after removing the machine noise. The force magnitude for each rotation in the background force experiment is shown in (Figure 6 e). The slight increase in force magnitude through time is due to an increase in friction between the lid and the outer cylinder with an increase of rotations. The background force magnitude is removed from the experimental results by subtracting the background force values from the force values obtained during experiments.

https://doi.org/10.5194/egusphere-2022-1004
Preprint. Discussion started: 6 October 2022

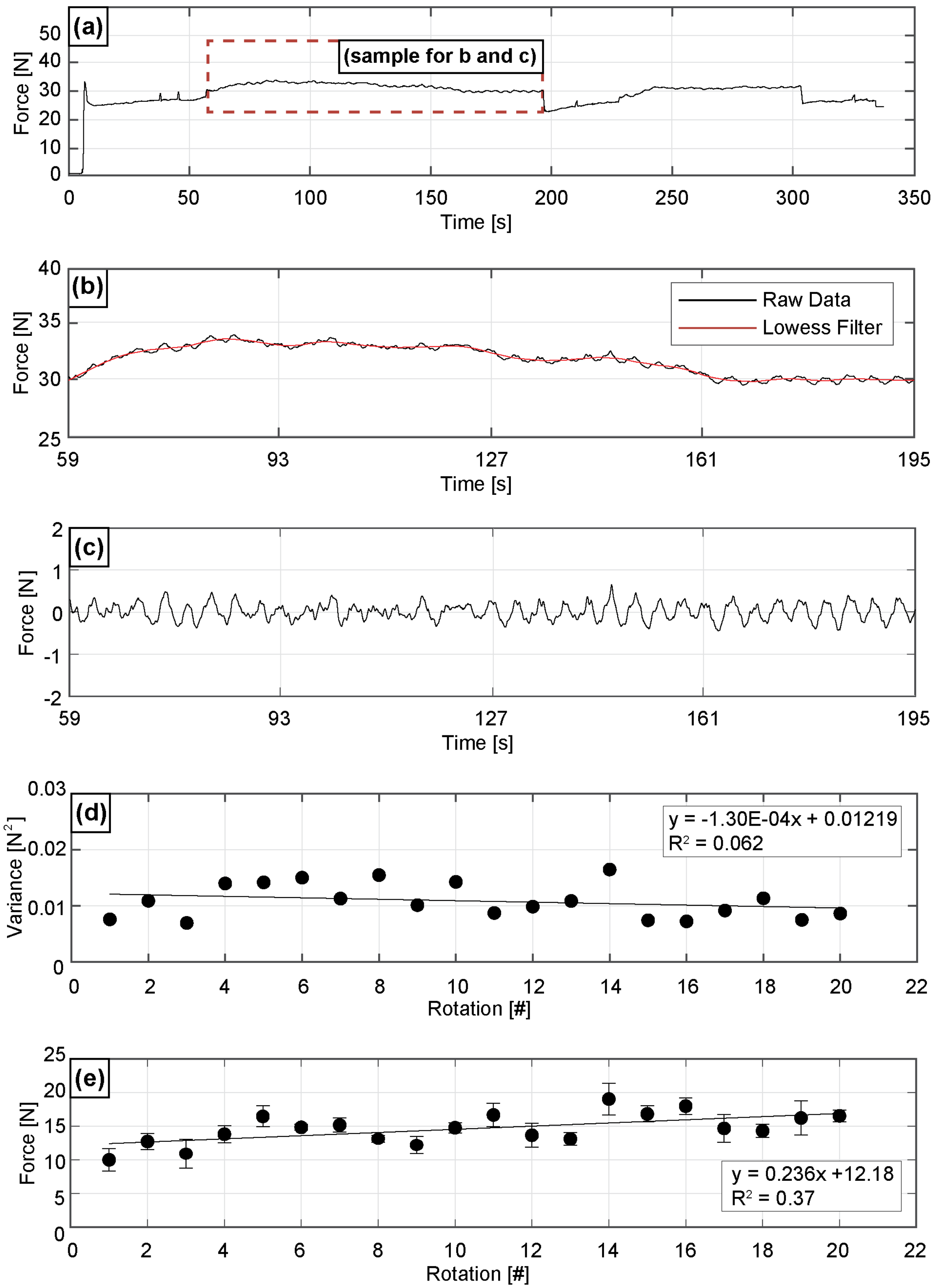

https://doi.org/10.5194/egusphere-2022-1004
Preprint. Discussion started: 6 October 2022

Figure 6: Filtering process. a) Raw force data from one rotation of the semi-brittle experiment with 64 vol% HydroOrbs. b) Sample of force data without large and recognizable signal noise. Black line: Raw force data, red line Lowess filter. c) Difference between the raw data and filtered data. d) Change in variance over 20 rotations. Variance associated with regular machine operation is calculated from each rotation in the background experiment (no deforming experimental material present in the experimental chamber). e) Change in pulling force magnitude over 20 rotations associated with regular ring shear operation of the background experiment (no deforming experimental material).

5 First experimental results

5.1 Results

We present results from three different experiments where we deform a granular material (HydroOrbs), a semi-brittle material (mixture of HydroOrbs and Carbopol), and a viscous material (Carbopol). The aim of this section is not to present results from a comprehensive parameter study but rather to give an overview of what types of experiments have been conducted so far on this new shear machine and to stimulate discussion on future use and improvements.

An angular velocity of 0.019 $\frac{rad}{sec}$ is used in all the experiments. Note, during an experiment the deformation strain rate can differ from the imposed rate of the machine due to the energy conserving boundary condition. The constant volume experiments are deformed by rotating the experimental chamber while the lid is held stationary. Figure 7 shows examples of the three types of experiments before deformation (left column) and after 20 rotations. The brittle HydroOrb experiment contains 2706 orbs. The pore space between the orbs is filled with air. Because air and the HydroOrbs have a different light refraction index we cannot utilise the laser sheet to visualize the internal deformation and are limited to observations from the outside (Figure 7 a and b). At the beginning of the experiment, all HydroOrbs are intact. They deform elastically when the normal force is applied but they do not fail. Note, the maximum confining pressure applied by the lid is 2 kPa and therefore less than the average yield stress of the HydroOrbs, which is at 25.44 kPa. With the start of deformation, individual orbs rearrange and start to fail and break into smaller pieces (Figures 3 and 7). This breaking happens predominantly during the first six rotations. Orb fragments accumulate in a layer in the middle of the experimental chamber. The filtered force curve of the brittle experiment shows multiple peaks and is overall noisy (Figure 8 a). The variance and the pulling force are both decreasing with an increase in number of rotations (Figure 8 d and e). The variance decreases from 0.2 N^2 to 0.1 N^2 over eighteen rotations. The pulling force decreases from approximately 30 N to 10 N.

The semi-brittle experiment contains 64 vol% HydroOrbs (2400 orbs) that are embedded in Carbopol. The Carbopol has a yield stress of 27.9 Pa and a viscosity of 236 Pa.s at a strain rate of 0.0207 s^{-1}. We follow the Carbopol preparation guidelines outlined in Birren and Reber (2019) and Di Giuseppe et al. (2015). To reduce the amount of bubbles entrapped in the Carbopol we directly mix the Carbopol in the experimental chamber. It is impossible to produce the Carbopol entirely bubble free. The shadow of these bubbles can be seen as dark horizontal lines in Figure 7 c and d. At the beginning of deformation, the majority of orbs are intact. Due to the mixing of the Carbopol, a few orbs can be damaged and show fractures. With increasing strain, some of the orbs start to fracture and break into smaller pieces. While some orbs break into two halves, others shatter (inset Figure 7d). At the end of the experiment approximately 6% of all orbs are broken in addition to orbs that broke during the

https://doi.org/10.5194/egusphere-2022-1004
Preprint. Discussion started: 6 October 2022

experiment preparation. The filtered force curve is relatively smooth and does not significantly differ from the background experiment (Figure 8 b). The variance and pulling force do not change significantly between rotations (Figure 8 d and e). The variance is low with 0.04 N^2 while a pulling force of approximately 34 N is relatively high.

The yield stress and viscosity of the Carbopol at experimental strain rate are 26.6 Pa and 225.7 Pa.s, respectively in the viscous experiment. Because the Carbopol is transparent we place mechanically passive markers in the gel to visualize deformation. Multiple strands of beads are added to the experiment at different locations between the two cylinders. One line of beads is located close to the outer wall of the experimental chamber, one in the middle and one close to the inner wall of the chamber. Because of the yield stress of the fluid, the beads are not sinking or rising. As expected, the lines of beads tilt with an increase in strain (Figure 7 e and f). We observe a shear band that accommodates the majority of the deformation just slightly below the teeth of the lid. The filtered data is rather smooth and does not show any prominent peaks (Figure 8 c). The variance shows no change with an increase in rotation (Figure 8 d). The pulling force required to deform the experiment is lowest of the three experiments with approximately 16 N and does not change with the amount of deformation (Figure 8 e).

5.2 Comparison and discussion of the experiment results

The brittle experiment is the only experiment that shows a significant decrease in variance and pulling force with an increase in number of rotations (Figure 8 d and e), which is the reason for using a non-linear trendline for the brittle data. The force data is also the noisiest of the three experiments. These observations can be attributed to the rearranging and breaking of orbs during deformation. Both processes can lead to a stick-slip like behaviour (e. g. Cain et al., 2001; Mair et al., 2002; Monzawa and Otsuki, 2003). Over multiple rotations, the force signal from the brittle experiment becomes smoother, which is illustrated in the decrease of the variance (Figure 8 d). We attribute this change to the breaking of orbs, where most orbs break during the first 5-6 rotations. The smaller orb pieces migrate towards the middle of the experimental chamber and form a band. A similar organization of grain fragments has previously been observed in high speed rotary experiments (Siman-Tov and Brodsky, 2018).

In comparison to the brittle experiment, both the semi-brittle and the viscous experiments show little change in the force magnitude and the variance with an increase in rotations. Despite the semi-brittle experiment containing closely packed orbs, their rearrangement and breaking have a minimal impact on the force measurement. As soon as the pore space between the orbs is filled with a fluid (Carbopol) the resultant force measurements resemble the measurements of the viscous experiment (Figure 8 d and e). This is alike to observations of slip dynamics in lubricated granular experiments where small amounts of fluid smooth the stick-slip signal of the deforming granular material (Reber et al., 2014; Higashi and Sumita, 2009; Huang et al., 2005).

https://doi.org/10.5194/egusphere-2022-1004
Preprint. Discussion started: 6 October 2022

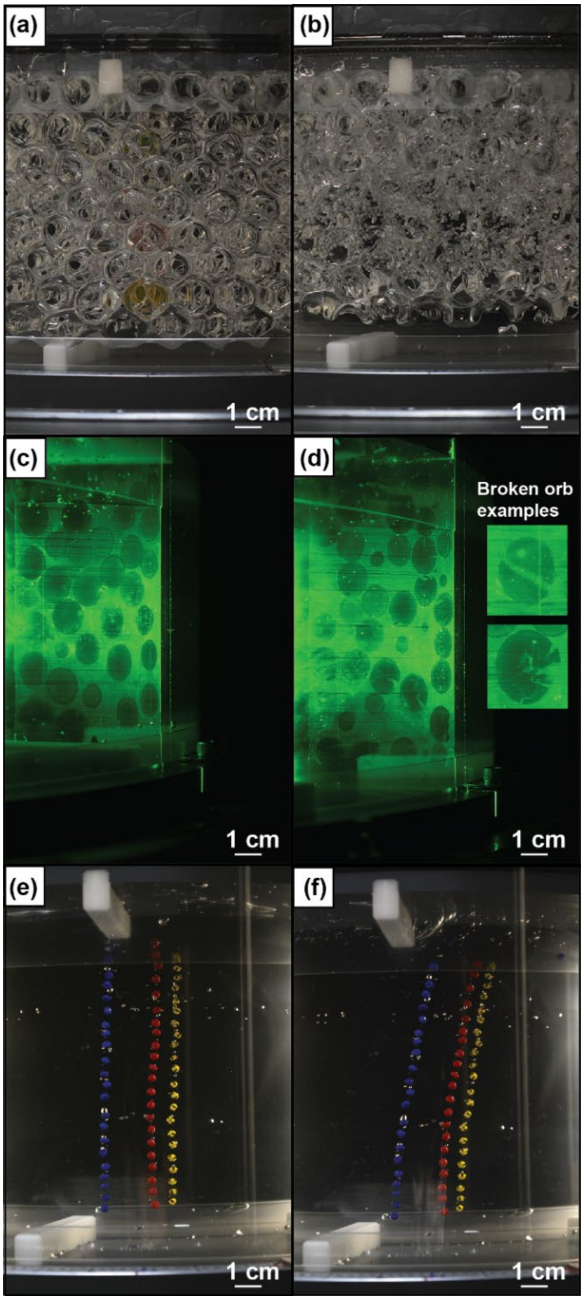

345 **Figure 7: Photographs of a brittle (a and b), semi-brittle (c and d), and viscous (e and f) experiment. Left column: at the beginning of the experiment before deformation, right column after 20 rotations.**

https://doi.org/10.5194/egusphere-2022-1004
Preprint. Discussion started: 6 October 2022

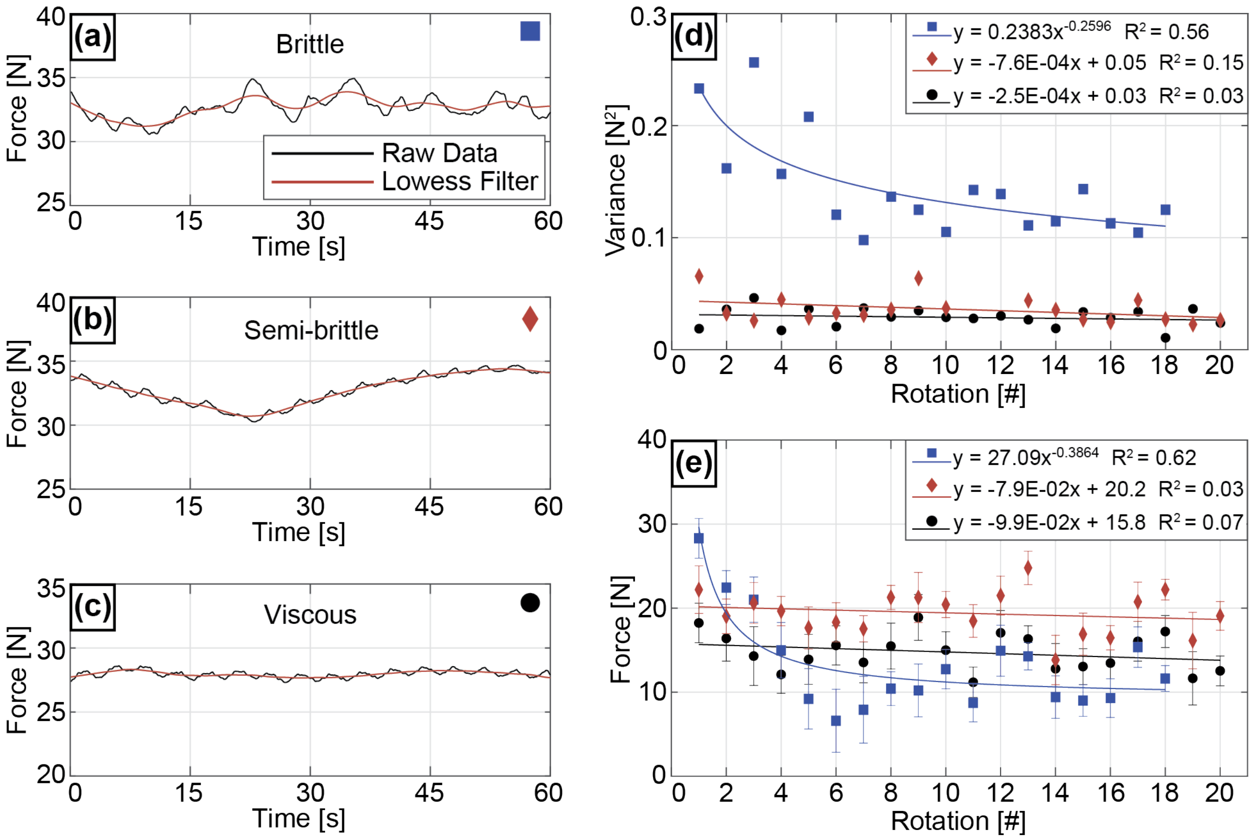

Figure 8: a) One-minute data sample of experiment deforming HydroOrbs (brittle). b) One-minute data sample of semi-brittle experiment where 64 vol% of HydroOrbs are embedded in Carbopol. c) One-minute data sample of experiment deforming Carbopol (viscous). Black line is the raw data. Red line is the smoothed data. d) Change in variance with rotations for brittle, semi-brittle, and viscous experiments. e) Change in pulling force with rotations brittle, semi-brittle, and viscous experiment.

6 Limitations, potential improvements, and additions

As with every experimental approach there are multiple levels of limitations. We will focus here on the limitations associated with the experimental apparatus. While the experimental materials have their limitations too, especially when it comes to scaling of experimental findings to geological applications, they are strongly dependent on the exact research question.

A big drawback of the machine is that force can only be measured as a bulk property. This means that it is hard to filter out all the machine noise. Furthermore, it remains impossible to record the force signal of a single breaking clast. Measuring the signal of an individual breaking clast would, however, be desirable especially for studies investigating the impact of failing brittle patches on slip dynamics. This could be addressed in the future by adding acoustic emission sensors into the experiment.

Another limitation is that the current design of the apparatus is unsuitable for experiments with a fluid that has a viscosity close to water. As the electrical motor is located at the same level as the bottom of the experimental chamber, leakage can become

https://doi.org/10.5194/egusphere-2022-1004
Preprint. Discussion started: 6 October 2022

a problem that would potentially harm the motor. Future shear apparatus designs should consider mounting the motor at the level of the lid and applying the confining pressure from the bottom if experiments with low viscosity fluids are planned. Furthermore, low viscosity fluids can also have a limiting impact on the applied normal force as they are more prone to leaking. Another limitation associated with the motor is that its strong electromagnetic field can impact the force gauge measuring the normal force leading to increased noise.

Illuminated sections through the experiment can only be produced in experiments filled with light refraction index matched materials. As soon as there is a non-index matched phase present (most commonly air) this type of observation in not possible anymore. Furthermore, currently only one cross-section can be analysed limiting the observation of the entire three-dimensional deformation.

7 Conclusion

We present the design of and first results from a new shear deformation apparatus for analogue multiphase experiments. The development of this experimental tool fills a gap in experimental capabilities to investigate multiphase deformation. The apparatus allows for recording deformation dynamics ranging from stick-slip to creep. The experimental setup is designed for observations to be made of the internal deformation of an experiment in progress, giving insight into the three-dimensional nature of deformation. For cross-sectional observation through the experimental chamber, experimental materials that are light refraction index matched are used. We introduce three different experimental materials that fulfil this requirement. First experiments using these materials show the variability of force measurements and deformation styles. The presented experimental strategy has the potential to shed light on multi-phase processes associated with multiple geo-hazards.

Data availability

All raw data can be provided by the corresponding author upon request.

Author contribution

SML, HB, KB conducted the experiments, SML, HB, KB and JER analysed the results, and JER conceived the apparatus idea and was responsible for the designing and building as well as student supervision. All authors have contributed to the writing and figure drafting of this article.

Competing interests

All authors declare that they have no conflict of interest.

Acknowledgment

All authors were supported by NSF CAREER Grant #1843676 to JER. We thank Terry Hermann for engineering help and Neal Iverson for insightful discussions on custom deformation apparatus designs.

References

Auernhammer, G. K., Fataei, S., Haustein, M. A., Patel, H. P., Schwarze, R., Secrieru, E., and Mechtcherine, V.: Transparent model concrete with tunable rheology for investigating flow and particle-migration during transport in pipes, Materials & Design, 193, 108673, https://doi.org/10.1016/j.matdes.2020.108673, 2020.

Behr, W. M. and Bürgmann, R.: What's down there? The structures, materials and environment of deep-seated slow slip and tremor, Philos Trans A Math Phys Eng Sci, 379, 20200218-20200218, 10.1098/rsta.2020.0218, 2021.

Behr, W. M., Gerya, T. V., Cannizzaro, C., and Blass, R.: Transient Slow Slip Characteristics of Frictional-Viscous Subduction Megathrust Shear Zones, AGU Advances, 2, e2021AV000416, https://doi.org/10.1029/2021AV000416, 2021.

Birren, T. and Reber, J. E.: The Impact of Rheology on the Transition From Stick-Slip to Creep in a Semibrittle Analog, Journal of Geophysical Research: Solid Earth, 124, 3144-3154, 10.1029/2018jb016914, 2019.

Bogatz, K.: Deformation of Brittle Clasts Within a Viscous Matrix: Field and Experimental Observations, M.S., Iowa State University, Ann Arbor, 75 pp., 2021.

Budwig, R.: Refractive-index matching methods for liquid flow investigations Experiments in Fluids, 17, 350-355, 10.1007/bf01874416, 1994.

Byron, M. L. and Variano, E. A.: Refractive-index-matched hydrogel materials for measuring flow-structure interactions, Experiments in Fluids, 54, 1456, 10.1007/s00348-013-1456-z, 2013.

Cain, R. G., Page, N. W., and Biggs, S.: Microscopic and macroscopic aspects of stick-slip motion in granular shear, Physical Review E, 64, 016413, 10.1103/PhysRevE.64.016413, 2001.

Chang, S., Kim, M., Oh, S., Min, J. H., Kang, D., Han, C., Ahn, T., Koh, W.-G., and Lee, H.: Multi-scale characterization of surface-crosslinked superabsorbent polymer hydrogel spheres, Polymer, 145, 174-183, https://doi.org/10.1016/j.polymer.2018.04.073, 2018.

Daniels, K. E. and Hayman, N. W.: Boundary conditions and event scaling of granular stick-slip events, in: Powders and Grains 2009, edited by: Nakagawa, M., and Luding, S., AIP Conference Proceedings, 567-570, 2009.

Di Giuseppe, E., Corbi, F., Funiciello, F., Massmeyer, A., Santimano, T. N., Rosenau, M., and Davaille, A.: Characterization of Carbopol hydrogel rheology for experimental tectonics and geodynamics, Tectonophysics, 642, 29-45, 10.1016/j.tecto.2014.12.005, 2015.

Dijksman, J. A., Brodu, N., and Behringer, R. P.: Refractive index matched scanning and detection of soft particles, Review of Scientific Instruments, 88, 051807, 10.1063/1.4983047, 2017.

Fagereng, A. and Sibson, R. H.: Melange rheology and seismic style, Geology, 38, 751-754, 10.1130/g30868.1, 2010.

Herschel, W. H. and Bulkley, R.: Konsistenzmessungen von Gummi-Benzollösungen, Colloid and polymer science, 39, 291-300, 10.1007/BF01432034, 1926.

Higashi, N. and Sumita, I.: Experiments on granular rheology: Effects of particle size and fluid viscosity, Journal of Geophysical Research-Solid Earth, 114, B04413 10.1029/2008jb005999, 2009.

Huang, N., Ovarlez, G., Bertrand, F., Rodts, S., Coussot, P., and Bonn, D.: Flow of wet granular materials, Physical Review Letters, 94, 10.1103/PhysRevLett.94.028301, 2005.

Ioannidi, P. I., Bogatz, K., and Reber, J. E.: The Impact of Matrix Rheology on Stress Concentration in Embedded Brittle Clasts, Geochemistry, Geophysics, Geosystems, 23, e2021GC010127, https://doi.org/10.1029/2021GC010127, 2022.

Ioannidi, P. I., Le Pourhiet, L., Agard, P., Angiboust, S., and Oncken, O.: Effective rheology of a two-phase subduction shear zone: Insights from numerical simple shear experiments and implications for subduction zone interfaces, Earth and Planetary Science Letters, 566, 116913, https://doi.org/10.1016/j.epsl.2021.116913, 2021.

https://doi.org/10.5194/egusphere-2022-1004
Preprint. Discussion started: 6 October 2022

Iverson, N. R., Hanson, B., Roger Le, B. H., and Jansson, P.: Flow Mechanism of Glaciers on Soft Beds, Science, 267, 80-81, 1995.

Iverson, R. M., Reid, M. E., Iverson, N. R., LaHusen, R. G., Logan, M., Mann, J. E., and Brien, D. L.: Acute sensitivity of landslide rates to initial soil porosity, Science, 290, 513-516, 10.1126/science.290.5491.513, 2000.

James, J. D., Ludwick, J. M., Wheeler, M. L., and Oyen, M. L.: Compressive failure of hydrogel spheres, Journal of Materials Research, 35, 1227-1235, 10.1557/jmr.2020.114, 2020.

Jammes, S., Lavier, L. L., and Reber, J. E.: Localization and delocalization of deformation in a bimineralic material, Journal of Geophysical Research: Solid Earth, 120, 10.1002/2015JB011890., 2015.

Kirkpatrick, J. D., Fagereng, Å., and Shelly, D. R.: Geological constraints on the mechanisms of slow earthquakes, Nature Reviews Earth & Environment, 2, 285-301, 10.1038/s43017-021-00148-w, 2021.

Klein, S., Gibert, M., Berut, A., and Bodenschatz, E.: Simultaneous 3D measurement of the translation and rotation of finite-size particles and the flow field in a fully developed turbulent water flow, Measurement Science and Technology, 24, 10.1088/0957-0233/24/2/024006, 2013.

Ladd, C. R. and Reber, J. E.: The Effect of a Liquid Phase on Force Distribution During Deformation in a Granular System, Journal of geophysical research. Solid earth, 125, n/a, 10.1029/2020JB019771, 2020.

Mair, K., Frye, K. M., and Marone, C.: Influence of grain characteristics on the friction of granular shear zones, Journal of Geophysical Research-Solid Earth, 107, 10.1029/2001jb000516, 2002.

Monzawa, N. and Otsuki, K.: Comminution and fluidization of granular fault materials: implications for fault slip behavior, Tectonophysics, 367, 127-143, https://doi.org/10.1016/S0040-1951(03)00133-1, 2003.

Mukhopadhyay, S. and Peixinho, J.: Packings of deformable spheres, Physical Review E, 84, 011302, 10.1103/PhysRevE.84.011302, 2011.

Parker, J. and Merati, P.: An Investigation of Turbulent Taylor-Couette Flow Using Laser Doppler Velocimetry in a Refractive Index Matched Facility, Journal of Fluids Engineering, 118, 810-818, 10.1115/1.2835513, 1996.

Reber, J. E., Cooke, M. L., and Dooley, T. P.: What model material to use? A review on rock analogs for structural geology and tectonics, Earth-Science Reviews, 202, 1-21, 2020.

Reber, J. E., Hayman, N. W., and Lavier, L. L.: Stick-slip and creep behavior in lubricated granular material: insights into the brittle-ductile transition, Geophysical Research Letters, 41, 3471-3477, 2014.

Rignot, E., Mouginot, J., Scheuchl, B., Broeke, M. v. d., Wessem, M. J. v., and Morlighem, M.: Four decades of Antarctic Ice Sheet mass balance from 1979–2017, Proceedings of the National Academy of Sciences, 116, 1095-1103, doi:10.1073/pnas.1812883116, 2019.

Siman-Tov, S. and Brodsky, E. E.: Gravity-Independent Grain Size Segregation in Experimental Granular Shear Flows as a Mechanism of Layer Formation, Geophysical Research Letters, 45, 8136-8144, https://doi.org/10.1029/2018GL078486, 2018.

Stocker, T. F. and others, a.: Climate Change 2013–The Physical Science Basis, IPCC AR5, 230, 2013.

Zoet, L. K. and Iverson, N. R.: A slip law for glaciers on deformable beds, Science, 368, 76-78, doi:10.1126/science.aaz1183, 2020.